



Two-dimensional detailed numerical simulation of ammonia/hydrogen/air detonation: hydrogen concentration effects and transverse detonation wave structure

S. Kohama¹ · T. Ito¹ · N. Tsuboi¹ · K. Ozawa¹ · A. K. Hayashi²

Received: 13 October 2023 / Revised: 4 May 2024 / Accepted: 9 May 2024 / Published online: 24 June 2024
© The Author(s), under exclusive licence to Springer-Verlag GmbH Germany, part of Springer Nature 2024

Abstract

Numerical simulations on ammonia/hydrogen/air detonation are performed using a detailed reaction model to investigate the cellular instability and detonation dynamics as a function of hydrogen content. The UT-LCS model that includes 32 species and 213 elementary reactions is used in the present simulations. The fifth-order target compact nonlinear scheme captured the unstable detonation dynamics and the complicated flow structure including the propagation of a sub-transverse wave. The simulation performed with different hydrogen dilutions shows that the detonation propagates at the Chapman–Jouguet velocity for all cases, and the cell size for the ammonia/hydrogen mixing ratio $\alpha = 0.3$ becomes approximately 10 times larger than that for $\alpha = 1.0$ (hydrogen/air mixture). A transverse detonation produces a finescale cellular structure on the computed maximum pressure history. This complex shock formation is similar to those of a spinning detonation and two-dimensional propane/oxygen detonation. The cellular irregularity increases with decreasing hydrogen content because ammonia destabilizes the detonation cellular structure with a reduced activation energy of more than approximately 8.

Keywords Detonation structure · Ammonia · Detailed chemical reaction · Numerical simulation

1 Introduction

Ammonia, which does not produce CO₂ during combustion, is one of the most promising renewable fuels for zero carbon emission [1, 2]. Ammonia also has the advantages of better transportation and storage compared with hydrogen because of the boiling temperature of 240 K under atmospheric pressure and liquefaction pressure of 20 atm at 293 K. Therefore, ammonia is a useful alternative fuel and has been studied to improve the combustion efficiency. However, ammonia has a low laminar flame velocity compared with hydrogen and

has some risks due to its high toxicity and corrosive nature. Therefore, the combustion process under a high-pressure environment and its detonation ability need to be studied to prevent severe accidents.

Ammonia has been studied for application in internal combustion engine systems. For example, Kurata et al. [3] successfully demonstrated NH₃–air combustion power generation, Reiter et al. [4] demonstrated a compression-ignition diesel engine using ammonia, and Mørch et al. [5] investigated the use of ammonia/hydrogen mixtures as an SI-engine fuel. However, there are limited available data for deflagration-to-detonation transition (DDT), and detonation propagation and structure for ammonia. Akber et al. [6] experimentally measured detonation cell size for ammonia/oxygen diluted by nitrogen and argon. The measured cell size varied widely between 24 mm (NH₃ + 0.05O₂) and 101 mm (NH₃ + 0.75O₂ + N₂) at an initial pressure in the range of 65–80 kPa. Mevel et al. [7] and Weng et al. [8] also measured detonation cell size in ammonia/oxygen and ammonia/nitrous oxide mixture; they reported a detonation cell size for stoichiometric ammonia/oxygen between 13.5 and 53.8 mm for an initial pressure in the range of 100–42.6 kPa. As for DDT, Thomas [9]

Communicated by G. Ciccarelli.

This paper is based on work that was presented at the 29th International Colloquium on the Dynamics of Explosions and Reactive Systems (ICDERS), Siheung, Korea, July 23–28, 2023.

✉ N. Tsuboi
tsuboi@mech.kyutech.ac.jp

¹ Department of Mechanical and Control Engineering, Kyushu Institute of Technology, Kitakyushu, Fukuoka, Japan

² Department of Mechanical Engineering, Aoyama Gakuin University, Sagamihara, Kanagawa, Japan

conducted experiments in a 7-mm stainless tube with a mixture of methane/ammonia/oxygen at an initial pressure of 1–7 atm. He also discussed the constant n related the induction length (L_{ign}) to the detonation cell size λ to predict $\lambda = 10\text{--}220\text{ mm}$ with $n = 60$ for an initial pressure of 50–500 kPa. Thomas et al. [10] also measured flame acceleration in an ammonia/hydrogen/air mixture; they reported a weak acceleration and no DDT in their experiments with a 150-mm-diameter and 30-m-long pipe. Jing et al. [11] observed flame acceleration and DDT for an ammonia/oxygen mixture in a 93-mm-diameter 14.8-m-length tube. For the stoichiometric ammonia/oxygen mixture and initial pressure of 1 atm, the DDT run-up distance was 5.05 m, 54.8 times the tube diameter. Li et al. [12] conducted flame acceleration and DDT experiments in nitrous oxide/ammonia with propane. Huang et al. [13] carried out experiments in a rotating detonation engine (RDE) with ammonia/oxygen in the annular chamber with a Laval nozzle. As for the numerical simulations, Zhu et al. [14] simulated DDT in a two-dimensional tube with repeated obstacles for ammonia/hydrogen/oxygen using OpenFOAM with Song et al.'s detailed chemistry model [15]. Zhu et al. [16] also simulated a one-dimensional detonation in ammonia/hydrogen/air to determine the effects of hydrogen addition on the pulsating instability mode using the same reaction model [15]. Fang et al. [17] simulated a 2D RDE with the uniform injection of ammonia/hydrogen/air mixture using OpenFOAM solver, and Sun et al. [18] simulated a 3D RDE with the uniform injection of ammonia/hydrogen/air mixture using the commercial code Fluent in these simulations; the equivalent ratio of ammonia to hydrogen is varied to study engine performance stability NO_x emissions and pressure gain performance. However, there are no existing experimental data that can be used to validate the simulation results.

The present study aims to investigate the detailed cellular structure and the detonation dynamics for ammonia/hydrogen/air. The present study performs two-dimensional inviscid simulations with a detailed chemistry model to investigate cellular instability and to study the effect of hydrogen dilution on thermicity, reduced activation energy, and the stability parameter.

2 Chemical reaction model

An appropriate chemical reaction model is necessary to simulate the ignition of ammonia under high-pressure and high-temperature conditions in the detonation reaction zone. Three candidate reaction models for the present simulation are selected: the UT-LCS model [19], the Konnov model [20], and the Okafor model [21]. These reaction models contain chemical species and elementary reactions that are important for ammonium oxidation. The UT-LCS model con-

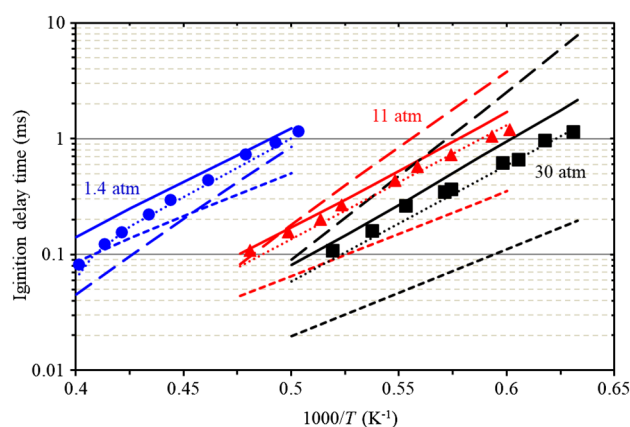


Fig. 1 Comparison of ignition delay time between numerical results and experimental data for stoichiometric ammonia/oxygen/Ar (0.005715NH₃/0.004285O₂/0.99Ar) gas mixture. Experimental values: filled circles, filled triangles, filled squares (Mathieu and Petersen [22]). Calculated values: solid line: UT-LCS model [19]; dotted line: UT-LCS model ($\tau_{\Delta T}$) [19]; long dashed line: Okafor model [21]; dashed line: Konnov model [20]

sists of 213 elementary reactions of 32 chemical species, the Konnov model consists of 1231 elementary reactions of 129 chemical species, and the Okafor model consists of 356 elementary reactions of 59 chemical species, respectively. Figure 1 shows a comparison of the 0D model ignition delay time for these reaction models and measurements from shock tube experiments [22]. The initial pressures are 1.4, 11, and 30 atm, and a stoichiometric ammonia/oxygen/Ar (0.005715NH₃/0.004285O₂/0.99Ar) gas mixture is used. Cantera library [23] is used to calculate the ignition delay time defined here as the maximum temperature gradient under adiabatic and constant volume conditions. In the shock tube experiment [22], the ignition delay time (τ_{OH^*}) was measured by the time-history OH*. Therefore, we also calculated the ignition delay time using the UT-LCS model and Otomo et al.'s simplified method [19], which calculates the elapsed time taken for the temperature to increase by 50 K from the initial temperature. These calculated values are plotted as $\tau_{\Delta T}$ (dotted line) in Fig. 1. Otomo et al. also calculated τ_{OH^*} by considering the excitation process of OH* and showed that $\tau_{\Delta T}$ agrees well with τ_{OH^*} [19]. Figure 1 shows that the ignition delay time for UT-LCS is close to that of the experiments for the three pressure conditions considered. The difference in ignition delay time between the two methods for UT-LCS is approximately two times, and $\tau_{\Delta T}$ agrees fairly well with the experiments [22], and we reproduce the results from [19]. However, the other two models are far from the experimental values. Therefore, we use the UT-LCS for the present detonation simulations.

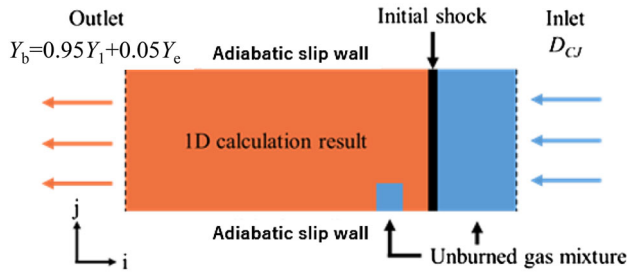


Fig. 2 Present calculation domain and boundary conditions

Table 1 Simulation conditions for various α

Case	1	2	3	4
α	0.3	0.5	0.8	1.0
C–J velocity (m/s)	1888.5	1911.7	1945.9	1968.4
C–J pressure (atm)	16.554	16.259	15.797	15.478
C–J temperature (K)	2731.8	2810.7	2891.4	2942.4
Grid width (μm)	60.7	22.8	6.42	4.22
Channel width (mm)	45.6	17.1	4.81	3.17
Channel length (mm)	151.1	57.1	16.1	10.5

3 Numerical method

3.1 Governing equations

The present governing equations are the two-dimensional Euler equations with the mass conservation equations and elementary reactions of 32 chemical species. The governing equations are as follows:

$$\frac{\partial \mathbf{Q}}{\partial t} + \frac{\partial \mathbf{E}}{\partial x} + \frac{\partial \mathbf{F}}{\partial y} = \mathbf{S} \tag{1}$$

$$\mathbf{Q} = \begin{pmatrix} \rho \\ \rho u \\ \rho v \\ e \\ \rho_1 \\ \vdots \\ \rho_N \end{pmatrix}, \quad \mathbf{E} = \begin{pmatrix} \rho u \\ p + \rho u^2 \\ \rho uv \\ (e + p)u \\ \rho_1 u \\ \vdots \\ \rho_N u \end{pmatrix},$$

$$\mathbf{F} = \begin{pmatrix} \rho v \\ \rho uv \\ p + \rho v^2 \\ (e + p)v \\ \rho_1 v \\ \vdots \\ \rho_N v \end{pmatrix}, \quad \mathbf{S} = \begin{pmatrix} 0 \\ 0 \\ 0 \\ \dot{\omega}_1 \\ \vdots \\ \dot{\omega}_N \end{pmatrix}, \tag{2}$$

where ρ is the density, u and v are the velocities along the x - and y -axis, respectively, p is the static pressure, and e is the total energy per specific volume; ρ_i denotes the density of each chemical species ($i = 1, 2, 3, \dots, N$), while $\dot{\omega}_i$ denotes the production rate of each chemical species. The following equations must always be satisfied:

$$\sum_{i=1}^N \rho_i = \rho, \quad \sum_{i=1}^N \dot{\omega}_i = 0. \tag{3}$$

Each species is assumed to satisfy the ideal gas equation of state:

$$p = \sum_{i=1}^N \rho_i R_i T = \sum_{i=1}^N \rho_i \frac{R}{W_i} T. \tag{4}$$

where R is the universal gas constant, R_i is the gas constant for each chemical species, and W_i is the molecular weight of each chemical species. The specific heat at constant pressure C_p , enthalpy h , and entropy S of each species for the standard-state atmosphere depends on the temperature as follows [24]:

$$\frac{C_p^i}{R_i} = a_{1i} + a_{2i} T + a_{3i} T^2 + a_{4i} T^3 + a_{5i} T^4, \tag{5}$$

$$\frac{h_i}{R_i T} = a_{1i} + \frac{a_{2i}}{2} T + \frac{a_{3i}}{3} T^2 + \frac{a_{4i}}{4} T^3 + \frac{a_{5i}}{5} T^4 + \frac{a_{6i}}{T}, \tag{6}$$

$$\frac{S_i^0}{R_i} = a_{1i} \ln T + a_{2i} T + \frac{a_{3i}}{2} T^2 + \frac{a_{4i}}{3} T^3 + \frac{a_{5i}}{4} T^4 + a_{7i}. \tag{7}$$

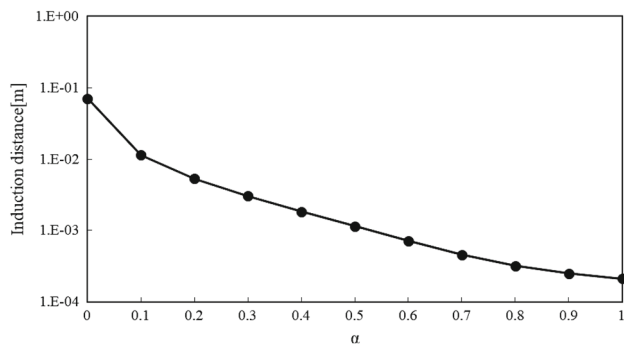


Fig. 3 Induction length calculated with the ZND model

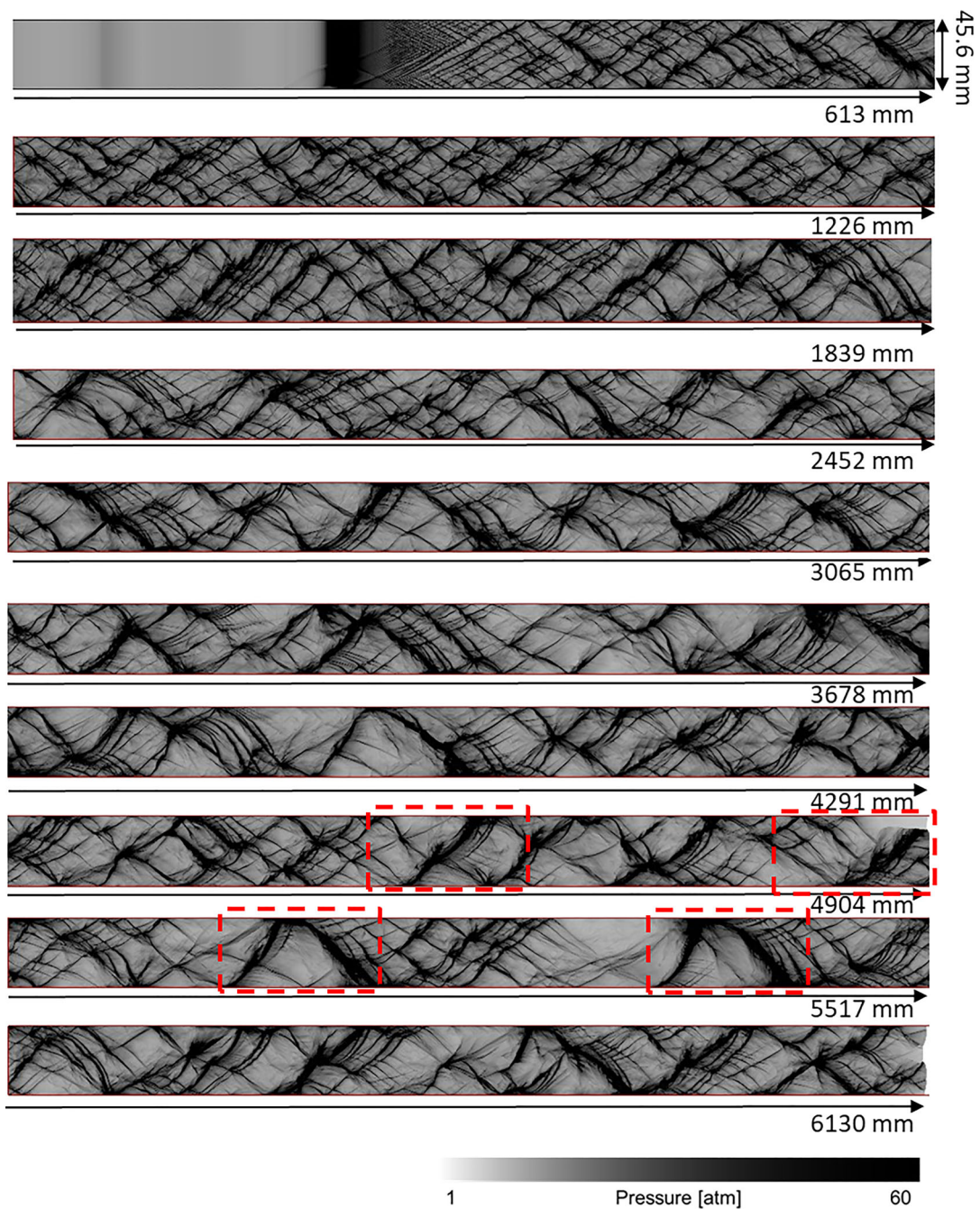


Fig. 4 Numerically obtained maximum pressure histories for $\alpha = 0.3$. Transverse detonation appears in the red dashed squares

The coefficients of each species, $a_{1i}, a_{2i}, \dots, a_{7i}$, are given by the JANAF table [25].

The total energy per unit volume e is defined as follows:

$$e = \sum_{i=1}^N \rho_i h_i - p + \frac{\rho}{2} (u^2 + v^2). \quad (8)$$

3.2 Chemical reaction model

A multi-step chain-branching chemical reaction mechanism, including the pressure dependence for each reaction rate coefficient, is used. The production rate of the i th species

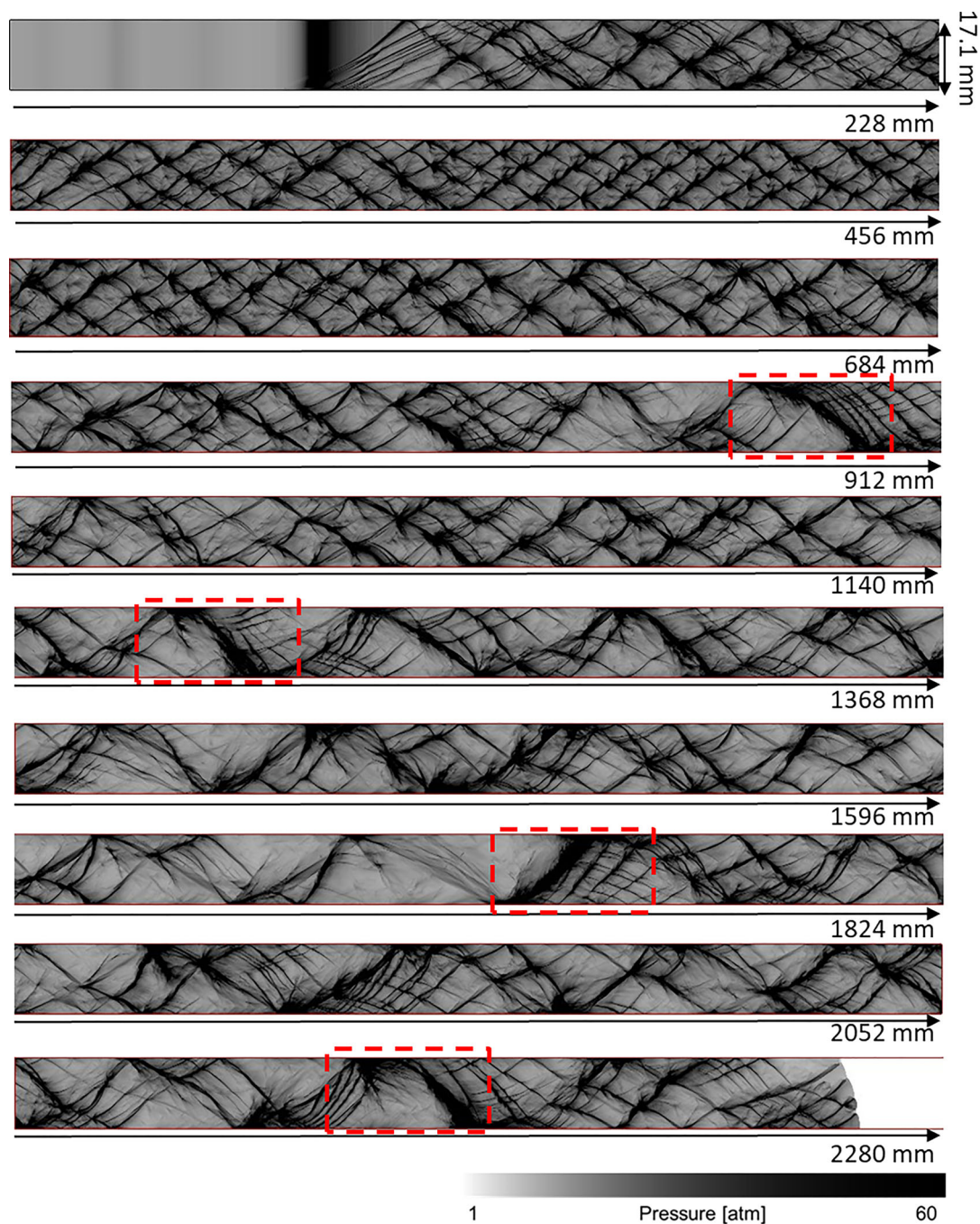


Fig. 5 Numerically obtained maximum pressure histories for $\alpha = 0.5$. Transverse detonation appears in the red dashed squares

$\dot{\omega}_i$ is calculated by

$$\dot{\omega}_i = W_i \sum_{k=1}^K (v''_{ik} - v'_{ik}) \left\{ k_{f,k} \prod_{i=1}^N [X_i]^{v'_{ik}} - k_{b,k} \prod_{i=1}^N [X_i]^{v''_{ik}} \right\}, \tag{9}$$

where v and X are the stoichiometric coefficient and molarity of each elementary reaction, respectively; k_f and k_b are the reaction rate coefficients of forward and backward elementary reactions, respectively. The reaction rate coefficient of each elementary reaction k is given by the following modified Arrhenius equation:

$$k = AT^n \exp\left(-\frac{E_a}{RT}\right), \tag{10}$$

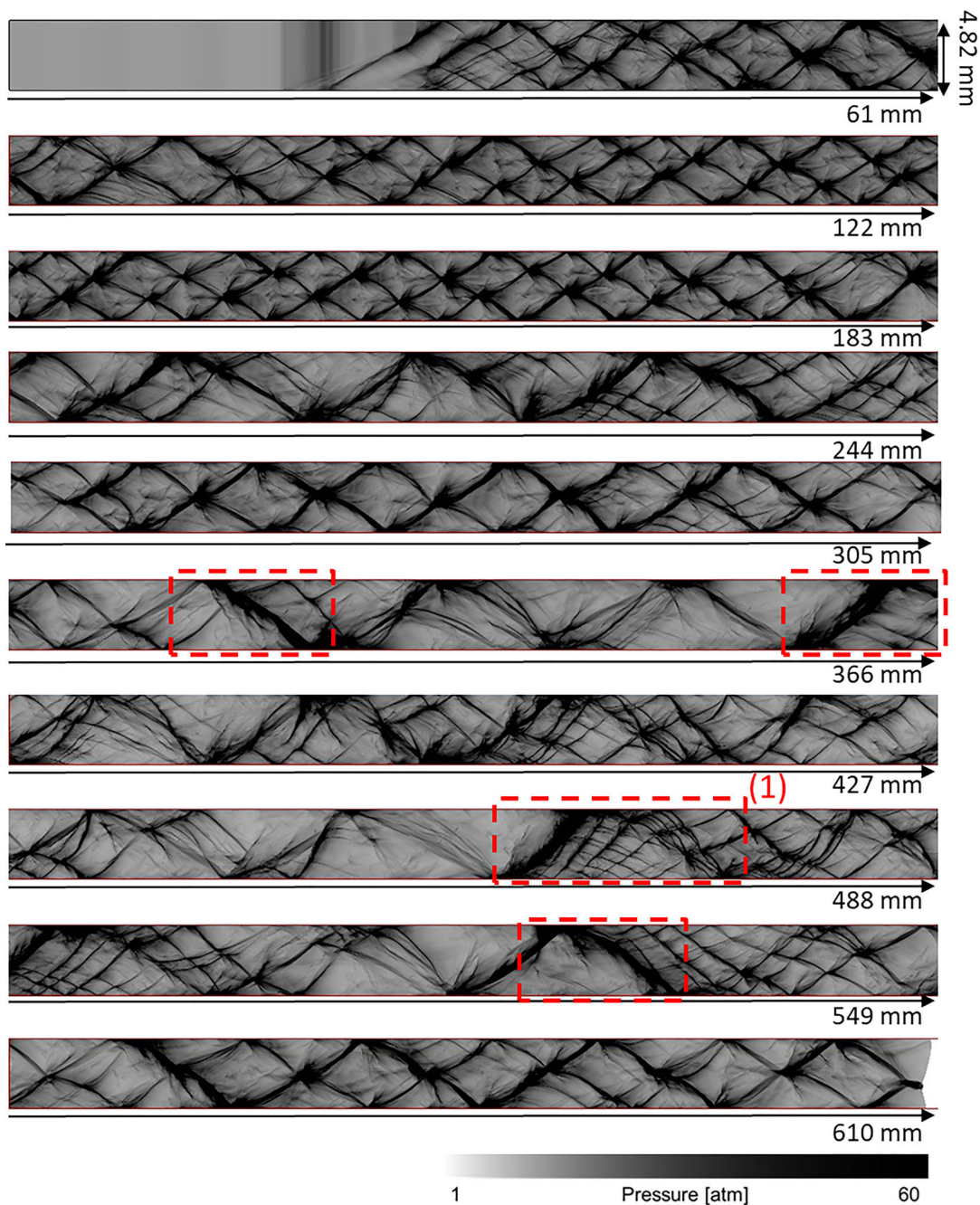


Fig. 6 Numerically obtained maximum pressure histories for $\alpha = 0.8$. Transverse detonation appears in the red dashed squares

where E_a is the activation energy. Some of the reaction rates include the pressure dependence and influence of third body M by the Lindemann, Troe formula, and PLOG function.

3.3 Numerical schemes

The two-dimensional compressible Euler equations with species conservation equations are solved by the following

numerical schemes. The numerical flux for the convective term uses the hybrid method combining the Harten–Lax–van Leer-contact (HLLC) [26] and the local Lax–Friedrich (LLF) schemes (HLLC/LLF scheme). Its accuracy is increased using the fifth-order target compact nonlinear scheme (TCNS) [27–35]. The authors previously simulated the detonation for hydrogen/air, hydrogen/oxygen, and propane/air mixtures using the fifth-order weighted compact nonlinear scheme (WCNS) in Ref. [31–33]; however,

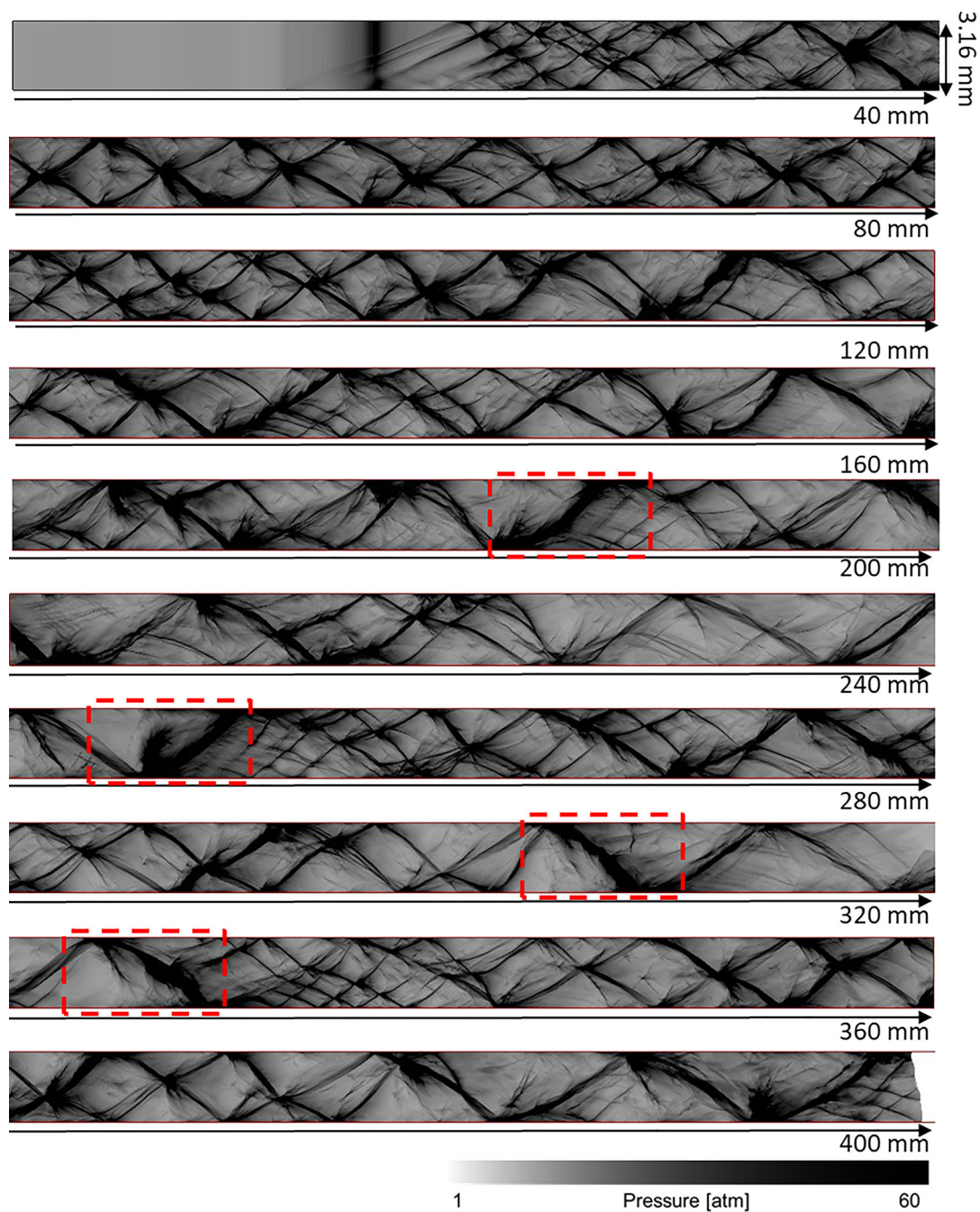
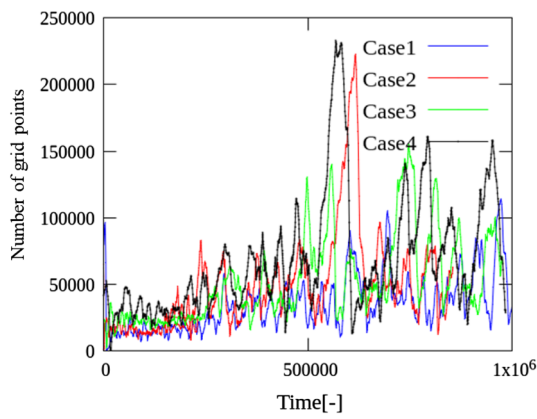


Fig. 7 Numerically obtained maximum pressure histories for $\alpha = 1.0$. Transverse detonation appears in the red dashed squares

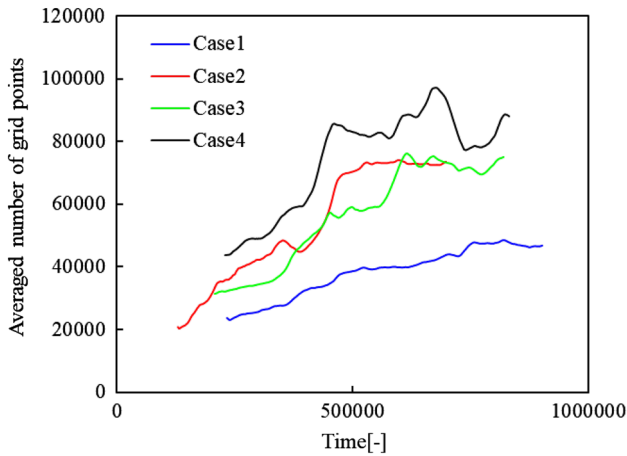
the present simulation uses the TCNS based on the targeted essentially non-oscillatory (TENO) scheme [34]. The difference between the WCNS and TCNS is the definition of the weighting function. The weighting function for the TCNS can be easily changed from that for the WCNS, and the present simulations use the TCNS. The fourth-order 10-step total variation diminishing (TVD) Runge–Kutta method [36] is used for the time integration method to increase numerical robustness. The chemical reaction source term is integrated

by the extended robustness-enhanced numerical algorithm (ERENA) [37]. The chemical reaction model adopts the UT-LCS model [19]. The Cantera library [23] is used to solve this chemical reaction because Cantera supports the PLOG function in this reaction model.

Figure 2 shows the numerical domain used for the study. The shock wave coordinate system is used to reduce the total calculation cost. The boundary conditions of the top and bottom walls are slip and adiabatic. Outlet condition at the



(a) Instantaneous distributions



(b) Moving averaged distributions with 100000 points

Fig. 8 Comparison of unburned gas area behind detonation front for various α

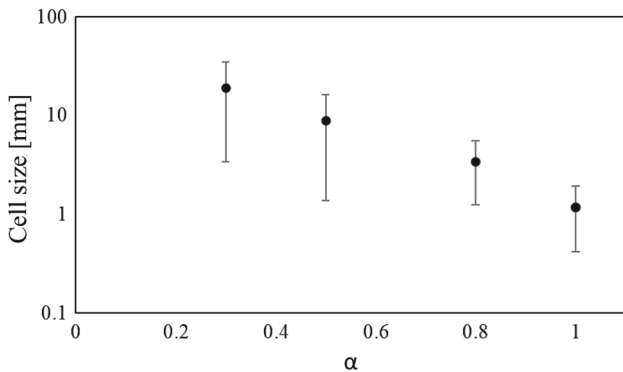


Fig. 9 Cell size for various α

left-side boundary is decided based on conditions proposed by Gamezo et al. [38]. The quantities Y_b , Y_1 , and Y_c in Fig. 2 refer to the value at the boundary ($i = 1$), the value at $i = 2$ near the boundary, and the ambient fluid value, respectively. The unburned gas is composed of $\text{NH}_3/\text{H}_2/\text{air}$ -premixed gas at 1 atm and 300 K. A small amount of burnt gas is placed behind the shock wave to create a small disturbance to initi-

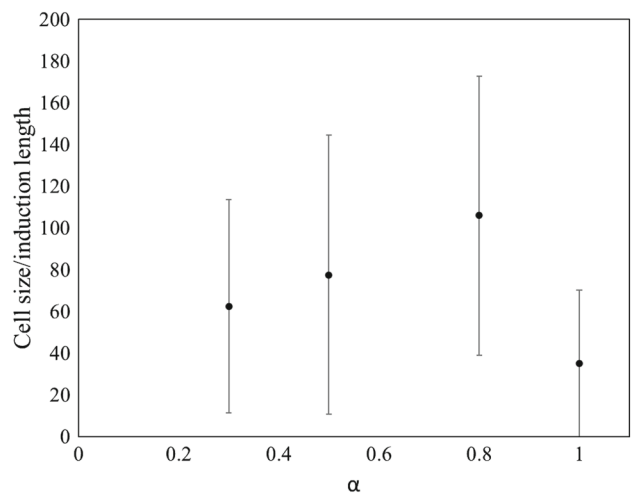


Fig. 10 Normalized cell size for various α

ate the detonation instability. The unburned gas enters at the Chapman–Jouguet (C–J) detonation velocity from the inlet side at the right boundary. The one-dimensional numerical results are also used to start the two-dimensional simulation.

Table 1 shows the simulation conditions of the present study, where the ammonia/hydrogen mixing ratio is varied by changing α :

$$4((1 - \alpha)\text{NH}_3 + 1.5\alpha\text{H}_2) + 3(\text{O}_2 + 3.76\text{N}_2). \quad (11)$$

The simulation for pure ammonia/air gas mixture ($\alpha = 0$) is not carried out because the detonation quickly quenches and is not self-sustained for the one-dimensional simulation. The grid width used for each case yields an induction length of 50 grid points. The induction lengths for various cases are calculated by Cantera, and the results are plotted in Fig. 3. The channel width should be selected according to the measured cell size. We first decided to set the channel width of the hydrogen/air gas mixture on the experimental data from Chen et al. [39]. As a reference, the detonation cell size of hydrogen/air was set to approximately 10 mm, and the channel width was set to approximately 0.3 times the detonation limit based on Chen et al.’s experimental data [39]. This means that the channel width in this simulation is 15 times the induction length. The present computational grid uses the orthogonal system, and the number of grid points for Case 4 (hydrogen/air in Table 1) is 3001×751 based on the total computational cost and required memory. Other ammonia/hydrogen/air mixtures (Cases 1–3) are also calculated with the same number of grid points as hydrogen/air (Case 4). The details of the grid width and channel width are listed in Table 1. The initial pressure and temperature were set to 1 atm and 300 K.

The two-dimensional numerical code is parallelized with MPI (message passing interface). These simulations are

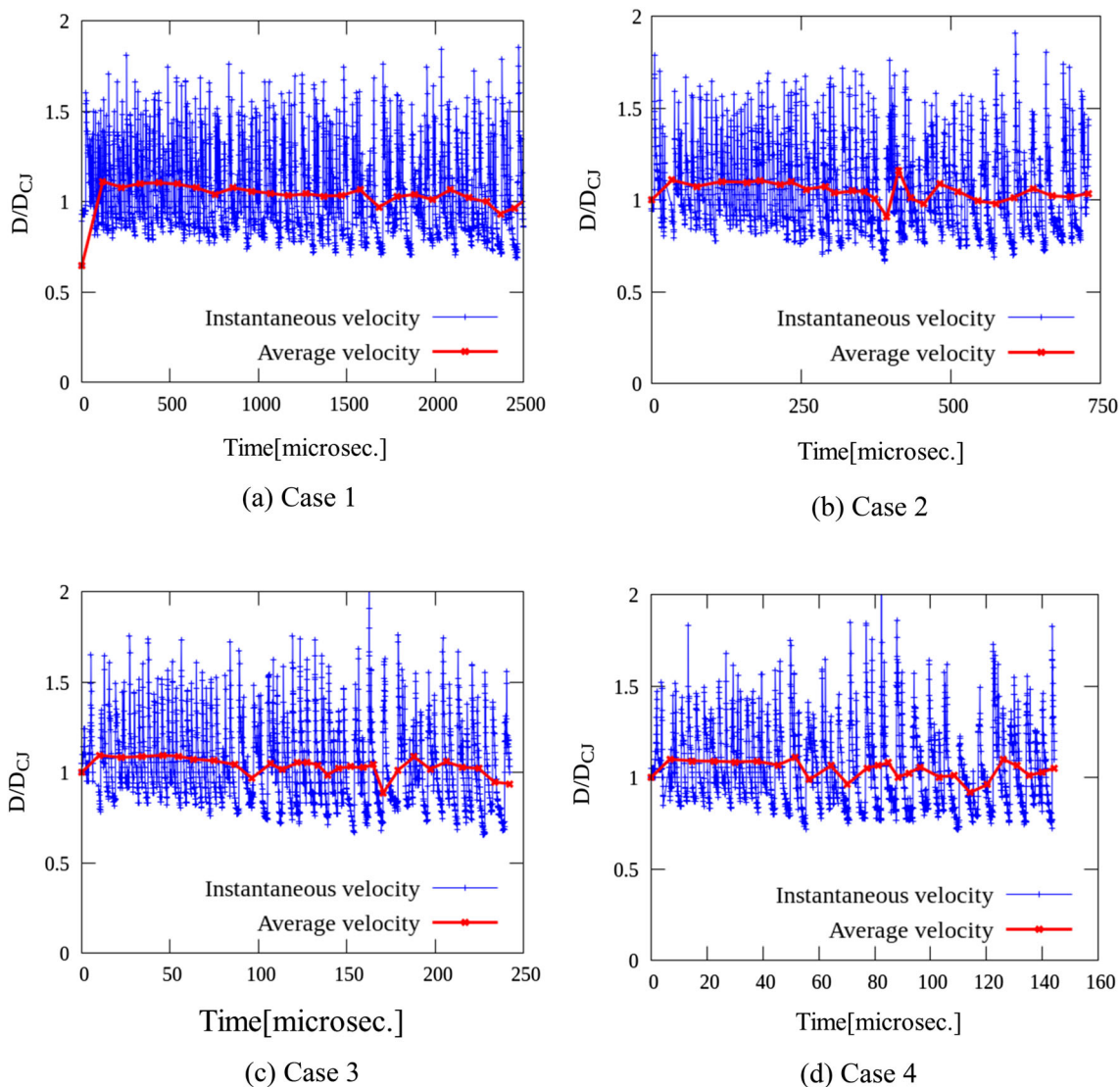


Fig. 11 Detonation velocities for various α

performed using the Oakbridge-CX at the University of Tokyo.

4 Results and discussion

The simulations are performed to study cellular detonation structure for various ammonia/hydrogen/air mixtures at standard pressure conditions in narrow channels. The present simulations are focused on detonation cellular dynamics and cellular instability.

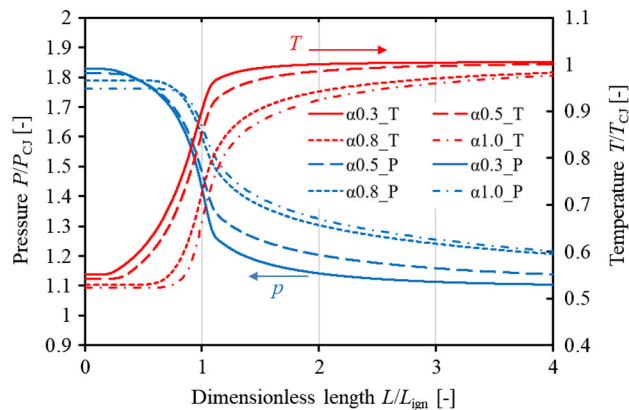


Fig. 12 Profiles of pressure and temperature for various α calculated with the ZND model

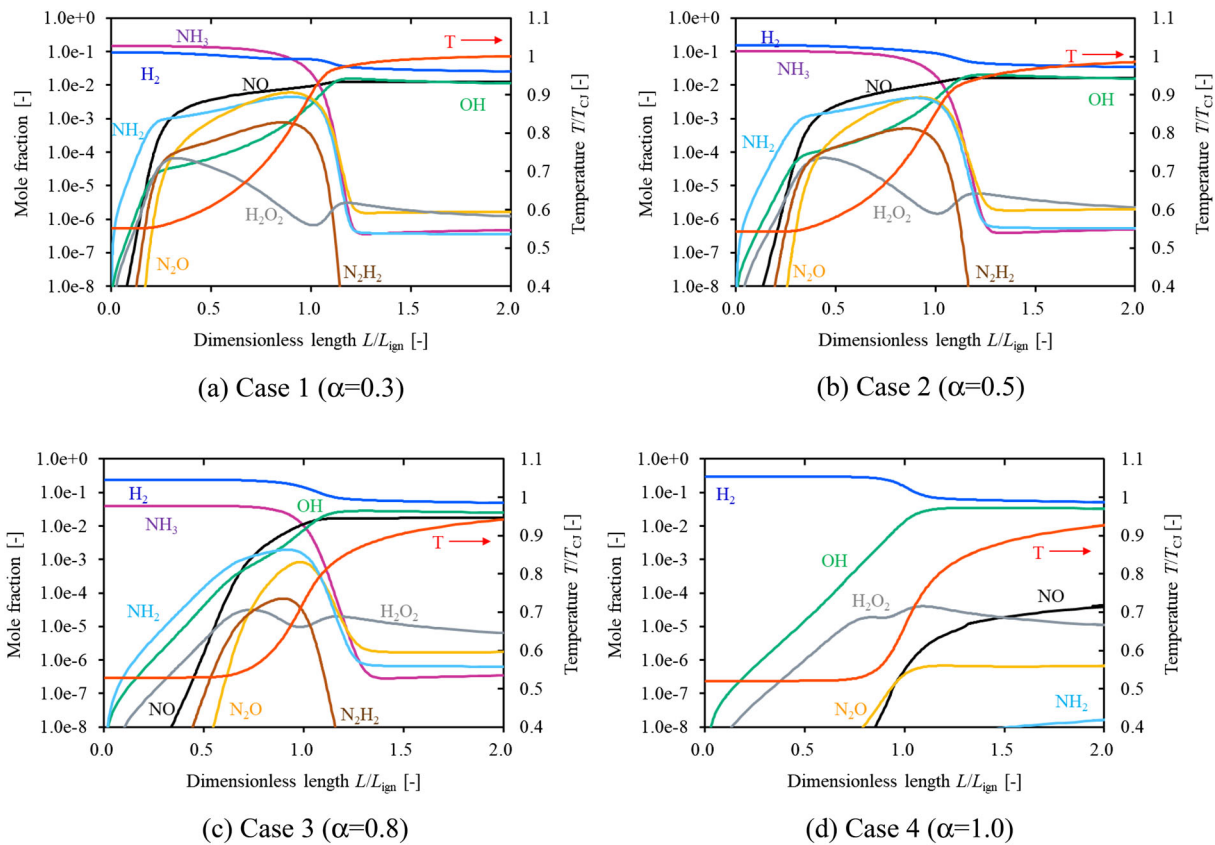


Fig. 13 Profiles of chemical species for various α calculated with the ZND model

4.1 Maximum pressure history and detonation velocities

The cellular structure is a key characteristic of a detonation wave. Figures 4, 5, 6, and 7 show the maximum pressure histories, analogous to experimental soot for cell structure

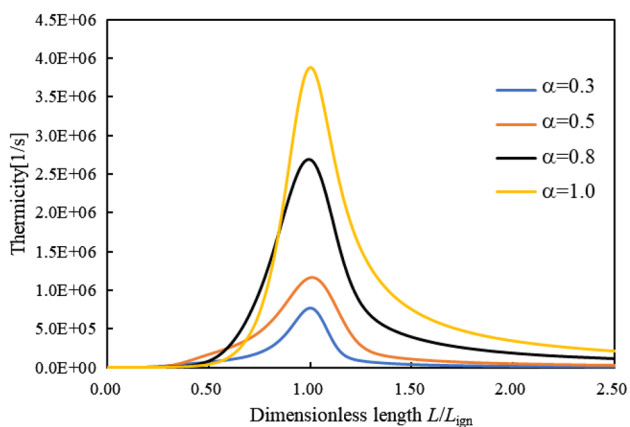


Fig. 14 Thermicity profiles near the detonation front calculated with the ZND model

imprint, for each case. The detonations for all cases persist beyond $L/d > 120$, where L is the propagation distance. The red dotted rectangle highlights the appearance of a transverse detonation in these figures. These figures show that the cellular structure becomes irregular with smaller cells as α decreases, i.e., the larger amount of ammonia produces irregular cellular structure. In Cases 3 and 4, the detonation propagates with a single-headed structure; however, Cases 1 and 2 show multiple transitions from a large cell size (single-headed) to a small cell size (multiple-headed) detonation structure. In the next section, the stability parameter is calculated for these conditions to understand the cell irregularity.

Figure 8 shows a comparison of the instantaneous and moving averaged unburned gas region behind the detonation front for all cases. The horizontal axis is normalized time, which is defined by $t_{\text{real}} \times D_{\text{CJ}} / \Delta_x$, where t_{real} is physical time and Δ_x is the grid width, respectively. The vertical axis denotes the total grid points in the unburned gas region because Cases 1–4 have the same total number of computational grid points. Figure 8a shows that the unreacted gas regions vary for all cases with a similar period. The moving averaged distributions of the unburned gas region in Fig. 8b show some quantitative differences. Case 1 ($\alpha = 0.3$) has the lowest distribution in all cases

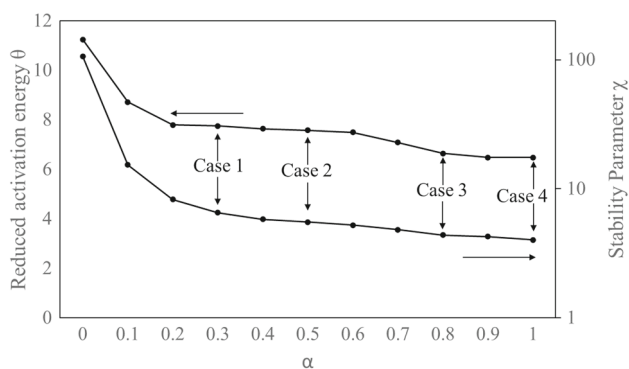


Fig. 15 Reduced activation energy and stability parameter calculated with the ZND model

because many transverse waves and a highly unstable detonation quickly consume unburned gas near the detonation front. The detonation for Case 4 ($\alpha = 1.0$, H_2/air mixture) produces a weakly unstable detonation with a larger unburned gas area, typically nearly stable detonation generates larger unburned gas regions. More simulations need to be done in the future to understand this feature.

The cell size (λ) and normalized cell size (λ/Δ_i) as a function of α are presented in Figs. 9 and 10, respectively. The vertical bars in these figures are standard deviations, which are obtained by the measured cell sizes in the maximum pressure histories in Figs. 4, 5, 6, and 7. For $\alpha = 1$ (hydrogen/air), the experimental cell size is approximately 10 mm, and the present results are smaller than the experimental data

because the present channel width $d = 3.17$ mm. The amount of hydrogen significantly affects the detonation cell size. The mean calculated cell size for $\alpha = 0.3$ is approximately 10 times larger than that for $\alpha = 1.0$. Because experimental cell size data for the ammonia/hydrogen/air mixture are not found in the literature, the validity of this feature will be verified in the future. The proportionality constant, $A = \lambda/\Delta_i$ in Fig. 10, shows a large deviation; however, the mean values are roughly in the range between 40 and 100. Westbrook et al. [40] proposed the linear correlation between the induction length and the cell size, and they showed that the value A depends on the mixture composition and equivalence ratio. Ng [41] also presented the value A from 3 to 100. The value of A for ammonia is not known.

Figure 11 shows the instantaneous (blue line) and averaged (red line) detonation velocities for various α . The detonations are self-sustained and do not quench, and the instantaneous detonation velocities vary between $0.7 D_{\text{CJ}}$ and $1.8 D_{\text{CJ}}$, where the average detonation velocity is approximately D_{CJ} .

4.2 ZND structure and stability parameter

Figure 12 shows the pressure and temperature calculated with the ZND model to understand the effects of hydrogen addition. Pressure and temperature profiles strongly depend on α , and the combustion behind the shock front starts faster with the increase in hydrogen addition.

Figure 13 shows the ZND profiles of the chemical species and temperature for various α . Behind the shock front, NH_2 is produced earlier than OH radical and NO because

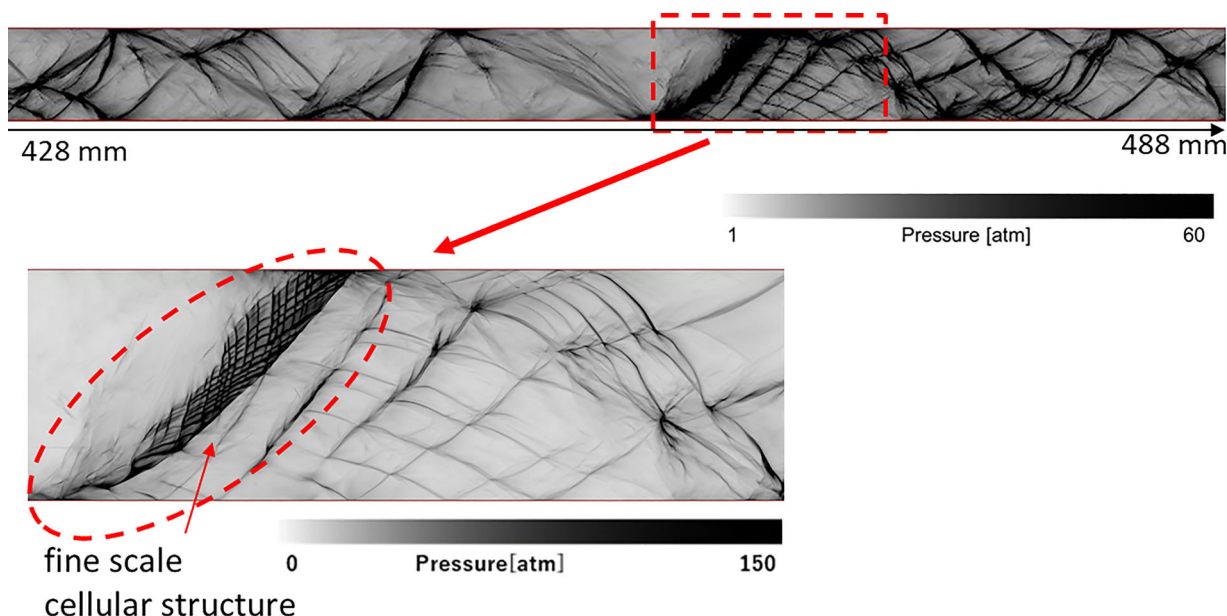


Fig. 16 Close-up view near the fine scale cellular structure on numerically obtained maximum pressure histories for $\alpha = 0.8$

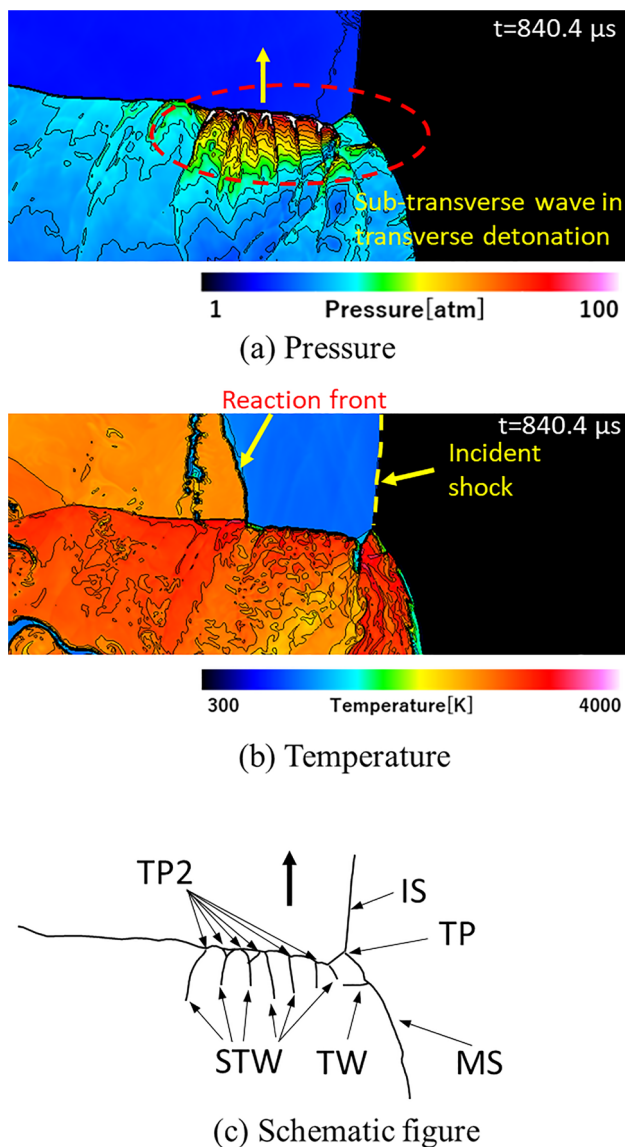


Fig. 17 Instantaneous pressure and temperature contours, and schematic figure near the transverse detonation; IS, MS, TP, TW, and STW denote incident shock, Mach stem, triple point, transverse wave, and sub-transverse wave, respectively

NH_3 decomposes first into NH_2 . Then, H_2O_2 , N_2H_2 , and N_2O are produced a little later. The radical OH and NO remain in the high-temperature region behind the combustion front; however, NH_2 , N_2H_2 , and N_2O decompose very quickly. These profiles show that NH_2 plays an important role in the concentration of NO [19]; however, NO does not decrease at $L/L_{\text{ign}} = 2.0$ for $\alpha = 0.8$ although maximum NH_2 decreases for $\alpha = 0.8$ because T_{CJ} is proportional to α .

A discussion about cellular structure stability is possible by using the one-dimensional ZND analysis, the reduced activation energy θ [42], and the stability parameter χ [43]. A large reduced activation energy produces an unstable detonation feature with the appearance and disappearance of the

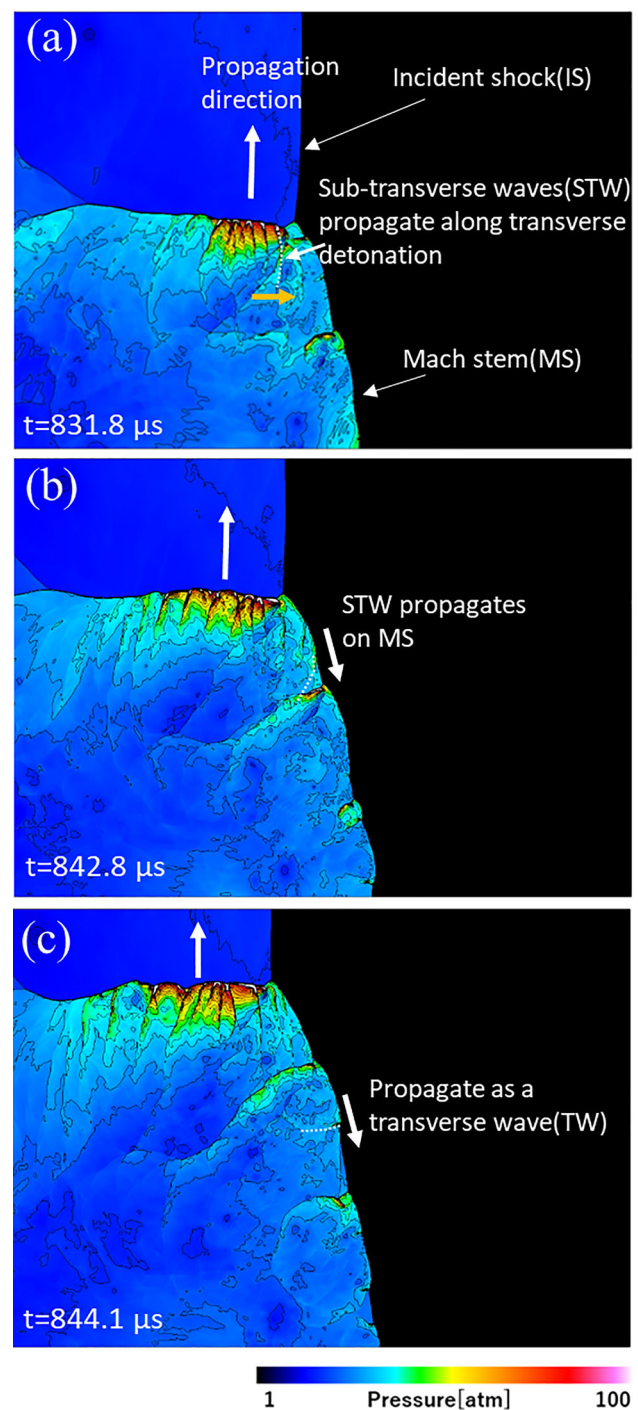


Fig. 18 Evolution of transverse detonation and sub-transverse waves

triple points by Gamezo et al. [38]. Ng et al. [43] also estimated the stability parameter for the various mixtures. The definition of the reduced activation energy θ and stability parameter χ is presented as follows:

$$\theta = \frac{E_a}{RT_{\text{vN}}} = \frac{1}{T_{\text{vN}}} \frac{\ln \tau_2 - \ln \tau_1}{\frac{1}{T_2} - \frac{1}{T_1}}, \quad (12)$$

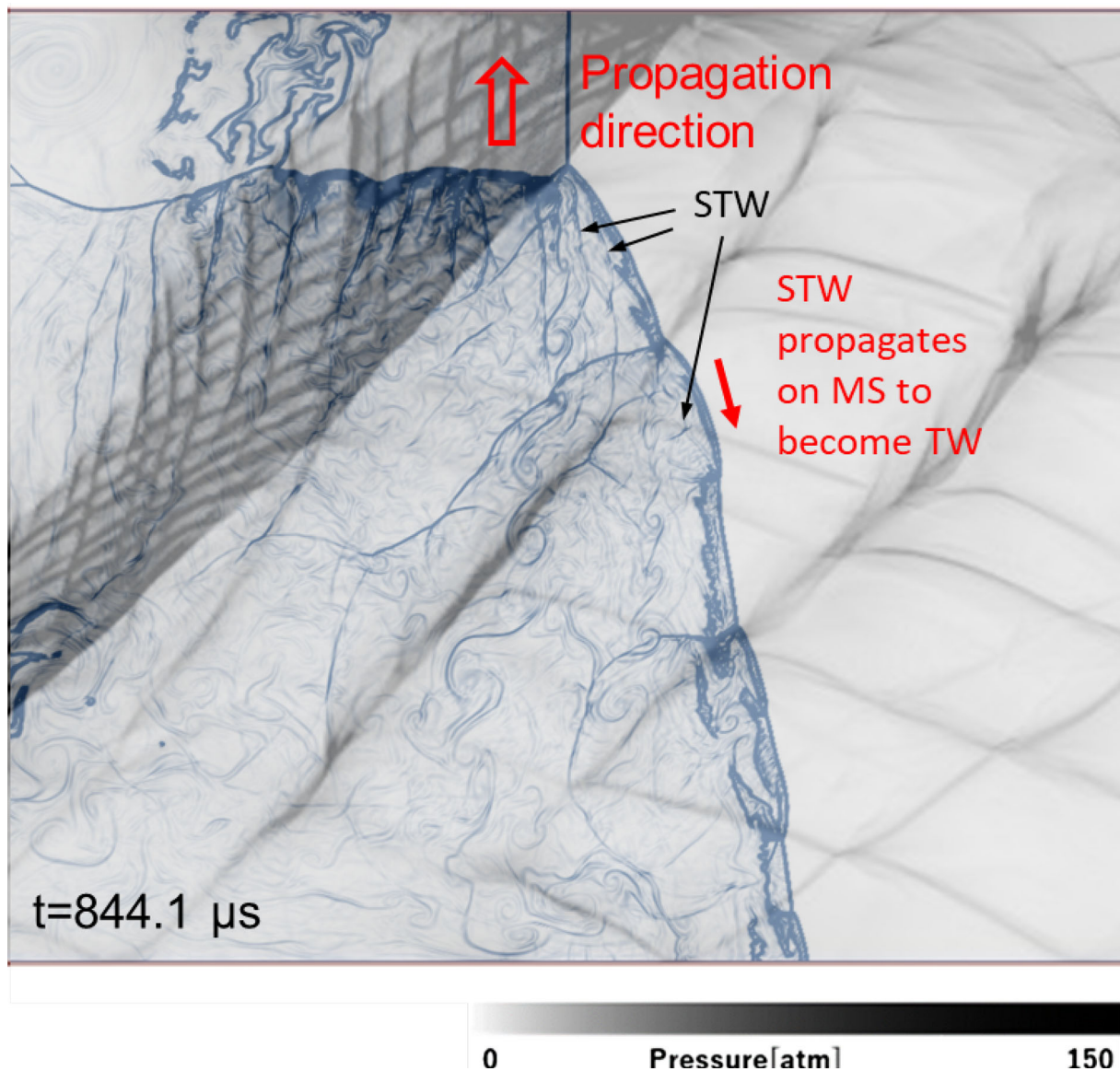


Fig. 19 Overlaid figures between instantaneous pressure contours and calculated maximum pressure histories near the transverse detonation

$$\chi = \theta \frac{\Delta_I}{\Delta_R} = \theta \Delta_I \frac{\sigma_{\max}}{u_{CJ}}, \quad (13)$$

where T_{vN} is the temperature behind the shock, (T_1, τ_1) and (T_2, τ_2) are temperature and induction time at a constant volume explosion analysis with $\pm 0.1\% D_{CJ}$. In (13), Δ_I and Δ_R are induction length and reaction length, and u_{CJ} is the CJ detonation velocity, and σ_{\max} is the maximum thermicity, respectively. The present results are also calculated by the UT-LCS [19]. Figure 14 shows the thermicity profile behind the detonation front as a function of α . This figure shows that the maximum thermicity σ_{\max} increases with increasing α (decreasing the amount of ammonia); however, the overall thermicity profile is not self-similar for all cases. There

is only one peak in the thermicity; there is no double peak structure observed in any of the cases.

Figure 15 shows the reduced activation energy θ and the stability parameter χ as a function of α . When hydrogen dilution increases, θ and χ decrease because the hydrogen reaction rate is higher and increases the cellular stability. These results indicate that the detonation cellular structure becomes regular with a large amount of hydrogen dilution. These results support the cellular instability feature in the two-dimensional simulation.

Manzhalei [44] proposed a minimum activation energy criterion of $\theta > 6.4$ to observe a substructure at the leading front of the detonation and to increase the detonation instability. Austin et al. [39] also discussed the effects of the

activation energy criterion in their experiments to support this criterion. The present estimation in Fig. 15 for $\alpha = 0.3$ (Case 1) and 0.5 (Case 2) shows that θ is approximately 8. Therefore, the cellular irregularity in the simulations increases with increasing ammonia.

4.3 Generation of new triple points and sub-transverse wave

Figure 16 shows the close-up view of region 1 in Fig. 6 (Case 4). The bottom figure in Fig. 16 shows a different pressure range from the top figure to enlarge the finescale cellular structure region. This finescale cellular structure region is produced by triple points in the transverse detonation (TD); note the TD mainly appears near the detonation propagation limit. This finescale cellular structure feature was also reported by the authors in a previous second-order simulation for propane/oxygen [34]; the present results are better resolved compared with the previous results [34]. This is because the present simulation uses a fifth-order scheme, whereas the previous propane/oxygen detonation simulation used a second-order scheme. The instantaneous pressure and temperature contours near the TD at $t = 840.4 \mu\text{s}$ are presented in Fig. 17. The schematic in Fig. 17c shows the detailed structure near the TD. This complicated shock interaction system is similar to that of a spinning detonation [45] and the propane/oxygen detonation [34]. Seven or eight triple points are observed in the TD. Figure 18 provides three instantaneous pressure contours showing the sub-transverse waves in the TD. One sub-transverse wave (STW) reaches the Mach stem at $t = 831.8 \mu\text{s}$ in Fig. 18a, and then, this STW propagates along the Mach stem at $t = 842.8 \mu\text{s}$ in Fig. 18b to become a transverse wave (TW) at $t = 844.1 \mu\text{s}$ in Fig. 18c. Figure 19 shows an overlay of the instantaneous density gradient at $t = 844.1 \mu\text{s}$ in Fig. 18c and the calculated maximum pressure history in Fig. 16. This figure shows that the STW causes the new TW on the calculated maximum pressure history. Asahara showed a similar feature that the STW on the TD propagates on the Mach stem [46]. As shown in Figs. 18 and 19, the STW is confirmed on the TD in this study as well. On the other hand, Asahara showed that the STW is caused by the micro-explosion that occurs at the junction of the reaction front and the TD. Such an explosion is not observed in this study, and some further calculations with finer grids are necessary in the future.

5 Conclusions

Numerical simulations on ammonia/hydrogen/air detonation are performed using a detailed reaction model to investigate the effect of hydrogen dilution on detonation stability and detonation dynamics. The conclusions are as follows:

- (1) The fifth-order TCNS scheme captured the unstable detonation dynamics and the complicated flow structure including a transverse detonation wave.
- (2) The simulation shows that the detonation propagates at the CJ velocity for all cases and the cell size for $\alpha = 0.3$ becomes approximately 10 times larger than that for $\alpha = 1.0$ (hydrogen/air mixture). The normalized cell sizes by the induction length show a large deviation; however, the mean values are in the range between 40 and 100.
- (3) The moving averaged distributions of the unburned gas region roughly depend on the amount of ammonia and cellular irregularity. The highly unstable detonation for $\alpha = 0.3$ quickly consumes the unburned gas near the detonation front; however, the weakly unstable detonation for $\alpha = 1$ (H_2/air) produces a larger unburned gas area because nearly stable detonation generates larger unburned gas regions.
- (4) A transverse detonation, which includes triple points and sub-transverse waves, creates a cross-hatching pattern on the computed maximum pressure history. This complex shock formation is similar to that of a spinning detonation.
- (5) The cellular irregularity increases with decreasing hydrogen dilution, i.e., ammonia destabilizes the detonation cellular structure with a reduced activation energy of more than 8.

Acknowledgements The authors would like to thank G. Inoue and N. Jourdain for their support of the present calculation code. The authors also appreciate Miyu Shimmoto and Daiki Kubota for their advice to calculate the ZND calculations. This study was carried out using the Oakbridge-CX system, which is a large-scale computing system of the University of Tokyo. The research is also supported by HPCI System Research project (Project ID: 180119, hp190082, and hp200044).

References

1. Elishav, O., Lis, B.M., Miller, E., Arent, D., Valera-Medina, A., Dana, A.G., Shter, G., Grader, G.: Progress and prospective of nitrogen-based alternative fuels. *Chem. Rev.* **120**(12), 5352–5436 (2020). <https://doi.org/10.1021/acs.chemrev.9b00538>
2. Kobayashi, H., Hayakawa, A., Kunkuma, K., Somarathne, A., Okafor, E.: Science and technology of ammonia combustion. *Proc. Combust. Inst.* **37**, 109–133 (2019). <https://doi.org/10.1016/j.proci.2018.09.029>
3. Kurata, O., Iki, N., Matsunuma, T., Inoue, T., Tsujimura, T., Furutani, H., Kobayashi, H., Hayakawa, A.: Performances and emission characteristics of NH_3 -air and NH_3 - CH_4 -air combustion gas-turbine power generations. *Proc. Combust. Inst.* **36**, 3351–3359 (2017). <https://doi.org/10.1016/j.proci.2016.07.088>
4. Reiter, A.J., Kong, S.C.: Demonstration of compression-ignition engine combustion using ammonia in reducing greenhouse gas emissions. *Energy Fuel* **22**, 2963–2971 (2008). <https://doi.org/10.1021/ef800140f>
5. Mørch, C.S., Bjerre, A., Gøttrup, M.P., Sørensen, S.C., Schramm, J.: Ammonia/hydrogen mixtures in an SI-engine: engine perfor-

- mance and analysis of a proposed fuel system. *Fuel* **90**, 854–864 (2011). <https://doi.org/10.1016/j.fuel.2010.09.042>
6. Akber, R., Kaneshige, M., Schultz, E., Shepherd, J.: Detonations in $H_2-N_2O-CH_4-NH_3-O_2-N_2$ Mixtures. Technical Report FM-97-3, Explosion Dynamics Laboratory, California Institute of Technology (1997)
 7. Mevel, R., Melguizo-Gavilanes, J., Chaumeix, N.: Detonation in ammonia-based mixtures. 11th Asia-Pacific Conference on Combustion, p. 249 (2017)
 8. Weng, Z., Mevel, R., Chaumeix, N.: Detonation in ammonia-oxygen and ammonia-nitrous oxide mixtures. *Combust. Flame* **251**, 112680 (2023). <https://doi.org/10.1016/j.combustflame.2023.112680>
 9. Thomas, G.O.: Flame acceleration and the development of detonation in fuel–oxygen mixtures at elevated temperatures and pressures. *J. Hazard. Mater.* **163**, 783–794 (2009). <https://doi.org/10.1016/j.jhazmat.2008.07.105>
 10. Thomas, G.O., Oakley, G., Bambrey, R.: An experimental study of flame acceleration and deflagration to detonation transition in representative process piping. *Process Saf. Environ. Prot.* **88**, 75–90 (2010). <https://doi.org/10.1016/j.psep.2009.11.008>
 11. Jing, Q., Huang, J., Liu, Q., Wang, D., Chen, X., Wang, Z., Liu, C.: The flame propagation characteristics and detonation parameters of ammonia/oxygen in a large-scale horizontal tube: As a carbon-free fuel and hydrogen-energy carrier. *Int. J. Hydrog. Energy* **46**, 191580–19170 (2021). <https://doi.org/10.1016/j.ijhydene.2021.03.032>
 12. Li, Y., Jiang, R., Xu, S.: Experimental studies on flame propagation and detonation characteristics of premixed nitrous oxide, ammonia, and propane in cylindrical channel. *Fuel* **334**, 126650 (2023). <https://doi.org/10.1016/j.fuel.2022.126650>
 13. Huang, S.Y., Zhou, J., Liu, S.J., Peng, H.Y., Yuan, X.Q.: Continuous rotating detonation engine fueled by ammonia. *Energy* **252**, 123911 (2022). <https://doi.org/10.1016/j.energy.2022.123911>
 14. Zhu, R., Zhao, M., Zhong, H.: Numerical simulation of flame acceleration and deflagration-to-detonation transition in ammonia–hydrogen–oxygen mixtures. *Int. J. Hydrog. Energy* **46**, 1273–1287 (2021). <https://doi.org/10.1016/j.ijhydene.2020.09.227>
 15. Song, Y., Hashemi, H., Christensen, J.M., Zou, C., Marshall, P.: Ammonia oxidation at high pressure and intermediate temperatures. *Fuel* **181**, 358–365 (2016). <https://doi.org/10.1016/j.fuel.2016.04.100>
 16. Zhu, R., Fang, X., Chao, X., Zhao, M., Zhang, H., Davy, M.: Pulsating one-dimensional detonation in ammonia–hydrogen–air mixtures. *Int. J. Hydrog. Energy* **47**, 21517–21536 (2022)
 17. Wang, F., Liu, Q., Weng, C.: On the feasibility and performance of the ammonia/hydrogen/air rotating detonation engines. *Phys. Fluids* **35**, 066133 (2023). <https://doi.org/10.1063/5.0152609>
 18. Sun, Z., Huang, Y., Luan, Z., You, Y.: Three-dimensional simulation of a rotating detonation engine in ammonia/hydrogen mixtures and oxygen-enriched air. *Int. J. Hydrog. Energy* **48**, 4891–4905 (2023). <https://doi.org/10.1016/j.ijhydene.2022.11.029>
 19. Otomo, J., Koshi, M., Mitsumori, T., Iwasaki, H., Yamada, K.: Chemical kinetic modeling of ammonia oxidation with improved reaction mechanism for ammonia/air and ammonia/hydrogen/air combustion. *Int. J. Hydrog. Energy* **43**, 3004–3014 (2018). <https://doi.org/10.1016/j.ijhydene.2017.12.066>
 20. Konnov, A.A.: Implementation of the NCN pathway of prompt-NO formation in the detailed reaction mechanism. *Combust. Flame* **156**, 2093–2105 (2009). <https://doi.org/10.1016/j.combustflame.2009.03.016>
 21. Okafor, E.C., Naito, Y., Colson, S., Ichikawa, A., Kudo, T., Hayakawa, A., Kobayashi, H.: Measurement and modeling of the laminar burning velocity of methane–ammonia–air flames at high pressures using a reduced reaction mechanism. *Combust. Flame* **204**, 162–175 (2019). <https://doi.org/10.1016/j.combustflame.2019.03.008>
 22. Mathieu, O., Petersen, E.L.: Experimental and modeling study on the high-temperature oxidation of ammonia and related NOx chemistry. *Combust. Flame* **162**, 554–570 (2015). <https://doi.org/10.1016/j.combustflame.2014.08.022>
 23. Goodwin, D.G., Speth, R.L., Moffat, H.K., Weber, B.W.: <https://www.cantera.org>, version 2.5.1 (2021)
 24. Kee, R.J., Rupley, F.M., Meeks, E., Miller, J.A.: CHEMKIN-III: a FORTRAN chemical kinetics package for the analysis of gas-phase chemical and plasma kinetics, Sandia National Lab. SAND-96-8216 (1996). <https://doi.org/10.2172/481621>
 25. Stull, D.R., Prophet, H.: JANAF Thermochemical Tables, 2nd edn. U.S. Dept. of Commerce, National Bureau of Standards, Washington, DC (1971)
 26. Toro, E.F., Spruce, M., Speares, W.: Restoration of the contact surface in the HLL-Riemann solver. *Shock Waves* **4**, 25–34 (1994). <https://doi.org/10.1007/BF01414629>
 27. Deng, X., Zhang, H.: Developing high-order weighted compact nonlinear schemes. *J. Comput. Phys.* **165**, 22–44 (2000). <https://doi.org/10.1006/jcph.2000.6594>
 28. Zhang, S., Jiang, S., Shu, C.-W.: Development of nonlinear weighted compact schemes with increasingly higher order accuracy. *J. Comput. Phys.* **227**, 7294–7321 (2008). <https://doi.org/10.1016/j.jcp.2008.04.012>
 29. Nonomura, N., Fujii, K.: Robust explicit formulation of weighted compact nonlinear scheme. *Comput. Fluids* **85**, 8–18 (2013). <https://doi.org/10.1016/j.compfluid.2012.09.001>
 30. Nonomura, T., Fujii, K.: Effects of difference scheme type in high-order weighted compact nonlinear schemes. *J. Comput. Phys.* **228**, 3533–3539 (2009). <https://doi.org/10.1016/j.jcp.2009.02.018>
 31. Nonomura, T., Iizuka, N., Fujii, K.: Freestream and vortex preservation properties of high-order WENO and WCNS on curvilinear grids. *Comput. Fluids* **39**, 197–214 (2010). <https://doi.org/10.1016/j.compfluid.2009.08.005>
 32. Niibo, T., Morii, Y., Asahara, M., Tsuboi, N., Hayashi, A.K.: Numerical study on direct initiation of cylindrical detonation in H_2/O_2 mixtures: effect of higher-order schemes on detonation propagation. *Combust. Sci. Technol.* **188**, 2044–2059 (2016). <https://doi.org/10.1080/00102202.2016.1215109>
 33. Iida, R., Asahara, M., Hayashi, A.K., Tsuboi, N.: Implementation of a robust weighted compact nonlinear scheme for modeling of hydrogen/air detonation. *Combust. Sci. Technol.* **186**, 1736–1757 (2014). <https://doi.org/10.1080/00102202.2014.935646>
 34. Takeshima, N., Ozawa, K., Tsuboi, N., Hayashi, A.K., Morii, Y.: Numerical simulations on propane/oxygen detonation in a narrow channel using a detailed chemical mechanism: formation and detailed structure of irregular cells. *Shock Waves* **30**, 809–824 (2020). <https://doi.org/10.1007/s00193-020-00978-5>
 35. Fu, L., Hu, X., Adams, N.A.: A family of high-order targeted ENO schemes for compressible-fluid simulations. *J. Comput. Phys.* **305**, 333–359 (2016). <https://doi.org/10.1016/j.jcp.2015.10.037>
 36. Gottlieb, S., Ketcheson, D.I., Shu, C.-W.: High order strong stability preserving time discretizations. *J. Sci. Comput.* **38**, 251–289 (2009). <https://doi.org/10.1007/s10915-008-9239-z>
 37. Morii, Y., Terashima, H., Koshi, H., Shimizu, T., Shima, E.: ERENA: a fast and robust Jacobian-free integration method for ordinary differential equations of chemical kinetics. *J. Comput. Phys.* **322**, 547–558 (2016). <https://doi.org/10.1016/j.jcp.2016.06.022>
 38. Gamezo, V.N., Desbordes, D., Oran, E.S.: Formation and evolution of two-dimensional cellular detonations. *Combust. Flame* **116**, 154–165 (1999). [https://doi.org/10.1016/S0010-2180\(98\)00031-5](https://doi.org/10.1016/S0010-2180(98)00031-5)

39. Chen, Y., Liu, B., Zhang, Y.P., Revankar, S.T., Tian, W.X., Qiu, S.Z., Su, G.H.: Effects of nitrogen and carbon monoxide on the detonation of hydrogen–air gaseous mixtures. *Nucl. Eng. Des.* **343**, 1–10 (2019). <https://doi.org/10.1016/j.nucengdes.2018.12.014>
40. Westbrook, C.K., Urtiew, P.A.: Chemical kinetic prediction of critical parameters in gaseous detonations. *Symp. Int. Combust.* **19**, 615–623 (1982). [https://doi.org/10.1016/S0082-0784\(82\)80236-1](https://doi.org/10.1016/S0082-0784(82)80236-1)
41. Ng, H.D.: The effect of chemical reaction kinetics on the structure of gaseous detonations. PhD Thesis, McGill University, Montreal (2005)
42. Austin, J.M., Printgen, F., Shepherd, J.E.: Reaction zones in highly unstable detonations. *Proc. Combust. Inst.* **30**, 1849–1857 (2005). <https://doi.org/10.1016/j.proci.2004.08.157>
43. Ng, H., Higgins, A., Kiyanda, C., Radulescu, M., Lee, J.H.S., Bates, K., Nikiforakis, N.: Nonlinear dynamics and chaos analysis of one-dimensional pulsating detonations. *Combust. Theory Model.* **9**, 159–170 (2005). <https://doi.org/10.1080/13647830500098357>
44. Manzhalei, V.I.: Fine structure of the leading front of a gas detonation. *Combust. Explos. Shock Waves* **13**, 402–404 (1977)
45. Tsuboi, N., Eto, K., Hayashi, A.K.: Detailed structure of spinning detonation in a circular tube. *Combust. Flame* **149**(1–2), 144–161 (2007). <https://doi.org/10.1016/j.combustflame.2006.12.004>
46. Asahara, M., Hayashi, A.K., Yamada, E., Tsuboi, N.: Generation and dynamics of sub-transverse wave of cylindrical detonation. *Combust. Sci. Technol.* **184**, 1568–1590 (2012). <https://doi.org/10.1080/00102202.2012.690324>

Publisher's Note Springer Nature remains neutral with regard to jurisdictional claims in published maps and institutional affiliations.

Springer Nature or its licensor (e.g. a society or other partner) holds exclusive rights to this article under a publishing agreement with the author(s) or other rightsholder(s); author self-archiving of the accepted manuscript version of this article is solely governed by the terms of such publishing agreement and applicable law.